Experiments on ceramic formation from liquid precursor spray axially injected into an oxy-acetylene flame

Alper Ozturk, Baki M. Cetegen *

Mechanical Engineering Department, University of Connecticut, 191 Auditorium Road, U-3139 Storrs, CT 06269-3139, USA

Abstract

An aqueous ceramic precursor solution was sprayed axially into an oxy-acetylene flame to produce yttria-stabilized zirconia ceramic deposits. Temperature and velocity fields of the oxy-acetylene flame were characterized by chemiluminescence and particle image velocimetry. Deposit samples were extracted from the flame at several downstream locations to study deposit evolution. The deposit phase and morphology were determined from Raman spectroscopy and scanning electron microscopy. Formation of the ceramic material commenced at around 4 cm distance from the injection point. The spectral peaks of the t′-phase of yttria-stabilized zirconia increased with increasing downstream distance whereas those of the precursor decayed.
© 2005 Acta Materialia Inc. Published by Elsevier Ltd. All rights reserved.

Keywords: Flame synthesis; Ceramics; Optical spectroscopy; Scanning electron microscopy; Raman spectroscopy

1. Introduction

Thermal barrier coatings (TBCs) have been widely used in industry to protect metallic components against high temperatures and high heat fluxes by applying an insulating layer of ceramic onto the metallic parts. Typically, turbine blades in gas turbine engines as well as the combustor liners are coated with TBCs. Application of TBCs provides longer service life for these components and allows higher gas path temperatures in modern high efficiency gas turbines (see review articles [1–3]).

Two commercial processes used for deposition of TBCs are the air-plasma spray (APS) and electron-beam physical-vapor deposition (EB-PVD). APS deposited coatings have lower thermal conductivities due to the porous coating microstructure generated in this process. This process is less costly than the EB-PVD process. However, EB-PVD coatings have superior durability over the APS coatings owing to the columnar microstructure that provides resistance to spallation caused by the thermal expansion mismatch between the ceramic and the superalloy substrate during thermal cycling.

The need for low-conductivity and low-cost thermal barrier coatings with high durability has led to research efforts on alternative deposition processes. The solution-precursor plasma-spray (SPPS) process has been introduced as a potentially low-cost process offering durable coatings with low thermal conductivities [4]. In the SPPS process, an aqueous solution containing yttrium and zirconium salts is injected into the plasma jet, in contrast to the APS process which utilizes ceramic powder as the feedstock material. The typical microstructure of SPPS coatings contains uniformly distributed porosity that contributes to the low thermal conductivity and evenly distributed vertical cracks which prolong the service life. SPPS coatings are also devoid of cracks running parallel to the surface which are omnipresent in the APS coatings. These horizontal cracks are detrimental to coating durability.

* Corresponding author. Tel.: +1 860 486 2966; fax: +1 860 486 5088.
  E-mail address: cetegen@engr.uconn.edu (B.M. Cetegen).

In order to build a fundamental understanding of ceramic formation in the SPPS process, a number of experiments have been conducted. Previous studies concentrated on the characterization of the single pass coatings and thick coatings using optical and scanning electron microscopy (SEM), X-ray diffraction (XRD) and thermal gravimetric analysis (TGA) [5–7]. Studies were extended to characterization of these coatings using scanning and transmission electron microscopy (TEM), X-ray diffraction and Fourier-transform infrared (FT-IR) spectroscopy analysis, in order to determine the process pathways to SPPS coating formation [8]. In addition, sample extraction experiments in the analysis of ceramic formation from individual electrostatically generated droplets were performed in a combustion flame environment. These experiments utilized high-speed droplet imaging, spectroscopic temperature measurements, and Raman and SEM analyses of flame-extracted samples [9]. These experimental studies were also accompanied by computational modeling efforts, in order to determine the precursor precipitation zones within individual droplets as these droplets penetrate into a very high temperature plasma environment and convect downstream [10,11].

Diagnostics of the SPPS process is made difficult due to the hostile plasma environment. High luminosity from the plasma makes droplet imaging extremely challenging. Most importantly, droplet spray is injected into the plasma transversely as it is not typically feasible to inject droplets axially into a plasma jet. As a consequence, the process involves different size droplets traversing different regions of the plasma jet. Particulates and droplets processed in the plasma jet typically contain material from the center of the jet as well as from the outer fringes of the plume resulting in both composition and morphology variations. Computational studies of transverse droplet injection into the plasma suggest that the highest temperatures experienced by these droplets are of the order of 2500 K [10]. It is possible to obtain similar temperatures in near stoichiometric oxy-fuel flames if droplets are injected axially into such a flame. Thus, the axial injection of droplets into an oxy-fuel combustion flame was considered in this study.

The precursor spray was generated and injected axially into an oxygen–acetylene flame to study the generation of ceramic deposits. Temperature and velocity measurements of the flame were first carried out to determine the thermal environment into which the droplets are injected. Droplet sizes and velocities were also measured in the absence of the flame to characterize the liquid precursor spray. Impact and thermophoretically collected samples were extracted in the flame at different downstream locations. These samples were evaluated using scanning electron microscope and Raman scattering for phase evolution with the increasing droplet residence time in the flame. In the following sections, we first describe the experimental systems employed in this study. This is followed by the presentation and discussion of the experimental results.

2. Experimental systems

A schematic of the experimental setup is shown in Fig. 1. The high temperature, premixed flame was obtained by modifying a commercial oxy-fuel cutting torch assembly. Commercial flame nozzle was replaced with a custom built nozzle that accommodated axial injection of precursor spray into the flame. Two mass flow controllers were used to accurately measure and control the oxygen and acetylene flow rates (Porter Instruments, Models 201-DKASVCAA and 251-DKASVCAA, Hatfield, PA). The oxygen and acetylene flow rates were adjusted to obtain a range of premixed flame stoichiometries. The nominal flow rates were $\dot{V}_{O_2} = 0.116$ L/s and $\dot{V}_{C_2H_2} = 0.051$ L/s. The equivalence ratio[1] corresponding to these oxygen and acetylene flow rates was selected as 1.1 based on the previous studies [9]. Theoretically, a stoichiometric mixture of acetylene and oxygen (corresponding to an equivalence ratio of 1) is expected to produce the highest temperature since complete combustion is attained without the dilution effect of excess air. However, it is well-known in the combustion literature [12] that maximum adiabatic flame temperature occurs at slightly fuel rich conditions, $\phi \approx 1.1$. Hence, a slightly fuel rich mixture was utilized in our experiments to produce the highest temperatures.

The precursor is a propriety composition of aqueous solution of yttrium and zirconium salts developed by Inframat Corporation (Willington, CT) and produces approximately 7 wt% yttria-stabilized zirconia upon deposition as a coating. Atomization of the precursor was accomplished by a miniature air-blast atomizer consisting of a 22-gauge stainless steel capillary pair positioned at right angle similar to those used by Tageldin and Cetegen [13]. The capillary tube that carries the nitrogen flow is aligned with the axis of the flame nozzle and the liquid is fed through the second capillary at right angle such that the nitrogen flow atomizes the precursor stream at the tip of the liquid-carrying capillary. In these experiments, the liquid precursor and atomizing nitrogen gas flow rates were set to 50 μL/s and 0.028 L/s, respectively. The liquid was fed into the atomizer by a syringe pump (KD Scientific, Model 200, Holliston, MA).

Measurement of flame temperatures is important in the study of precursor decomposition and ceramic for-

---

[1] The equivalence ratio is defined as fraction of fuel–air ratio of the combusting gases to that of a stoichiometric composition, or, $\phi = \frac{\dot{m}_f / \dot{m}_o}{(\dot{m}_f / \dot{m}_o)_{st}}$.
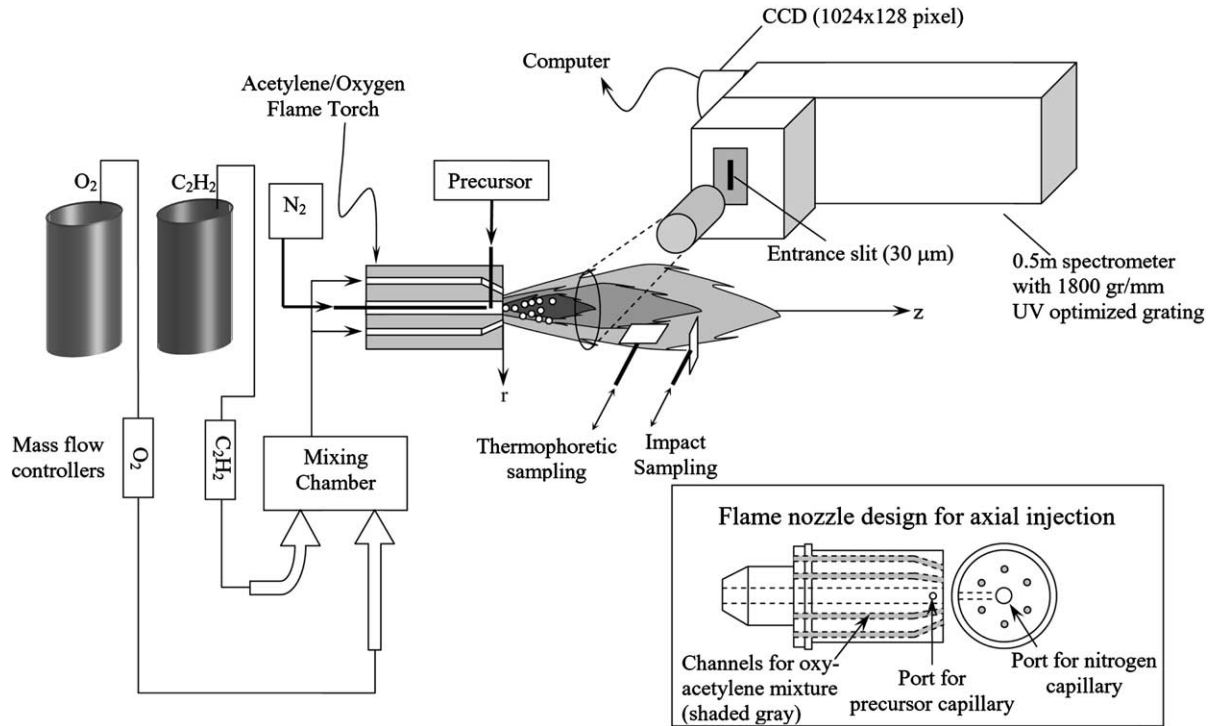
Fig. 1. Schematics of the experimental setup.

mation. In this study, temperature field was measured from chemiluminescence of the OH radical that is naturally present in the flame. This technique was chosen since thermocouple probing techniques are not readily applicable to the high temperatures of oxy-fuel flames. Rotational transition band of OH radical $A^2\Sigma^+ \rightarrow X^2\Pi(0,0)$ contains several emission branches that can be used to determine temperature. Here, several transition lines from the Q_1 branch of the bandhead at 305.356 nm were utilized in constructing Boltzmann plots from which temperatures were calculated [14]. One should note that only rotational transitions are considered in this study. Thermally induced vibrational and electronic transitions are not significant under flame conditions and one can approximate the rotational temperature as the actual temperature by neglecting vibrational and electronic contributions [15].

Intensity of emitted light from a particular transition, $j \rightarrow j'$, is expressed as

$$I_{jj'} = \frac{A S_{jj'}}{\lambda_{jj'}^4} e^{-E_j/kT}, \tag{1}$$

where $I_{jj'}$ is the intensity of the transition under consideration, $\lambda_{jj'}$ is the wavelength of the emitted light, $S_{jj'}$ is the Hönl–London coefficient, E_j is the transition energy and k is the Boltzmann constant. A plot of $\ln(I_{jj'}\lambda_{jj'}^4/S_{jj'})$ as a function of E_j/k, referred to as the Boltzmann plot, yields a linear relationship, the slope of which is $-1/T$. Wavelength, $\lambda_{jj'}$, Hönl–London coefficient, $S_{jj'}$, and transition energy, E_j, values are available in the litera-

ture [15] for several Q_1 branch transitions and properties of transitions used in this study are tabulated in Table 1. Characterization of the flame temperatures was accomplished by an imaging spectrometer (Acton Research, SpectraPro 500i). The spectrometer image was recorded by a 1024×128 pixel back-thinned CCD detector and image analysis was performed using WinSpec software. The spectral resolution was $\Delta\lambda_{app} = 0.03$ nm with 1800 gr/mm UV optimized grating and 30 μm slit width. Line-of-sight integrated intensities were deconvoluted into radial variations employing Abel's inversion [16]. Subsequently, Boltzmann plots were constructed for the Abel-inverted spectral intensities to calculate temperatures. In Fig. 2, three examples are plotted from the deconvoluted intensities. The temperatures shown in these plots correspond to temperatures of 3318, 3609 and 3909 K. The linearity of the experimental data

Table 1
Characteristics of OH emission lines used in temperature measurements [15]

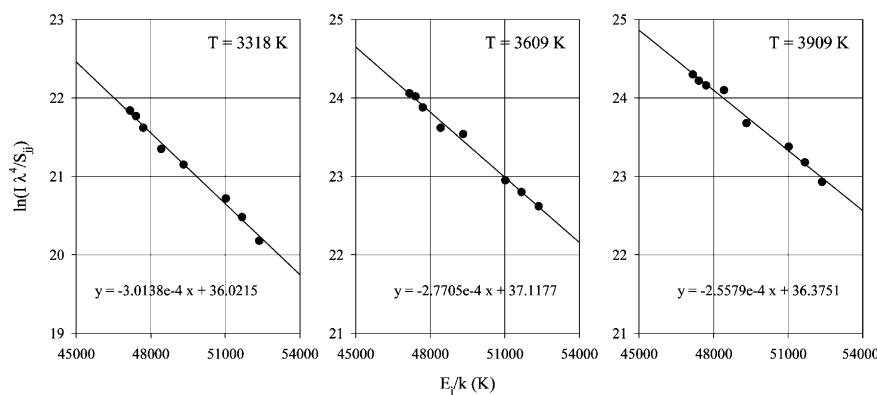|	$\lambda_{jj'}$ (nm)	E_j (cm^{-1})	$S_{jj'}$
$Q_1(4)$	308.417	32779.49	33.7
$Q_1(5)$	308.609	32948.31	42.2
$Q_1(6)$	308.823	33150.14	50.6
$Q_1(8)$	309.329	33652.29	67.5
$Q_1(10)$	309.910	34282.99	84.1
$Q_1(13)$	311.112	35462.01	108.8
$Q_1(14)$	311.567	35914.82	117.0
$Q_1(15)$	312.057	36396.66	125.2

Fig. 2. Typical Boltzmann plots obtained from the Abel-deconvoluted intensities showing temperatures of 3318, 3609 and 3909 K.

points suggest that the energy populations were in equilibrium.

Velocity distribution of the droplets and/or particulates in the flame was obtained by particle image velocimetry (PIV). The system consisted of a dual cavity Nd:YAG laser (Continuum Inc, Model: Surelite I-10, Santa Clara, CA), a 1300×1024 pixel frame-transfer CCD camera capable of double image feature (DIF) mode (Princeton Instruments, MicroMax 5 MHz, Trenton, NJ), a process timing unit (Stanford Research Systems Inc, DG535, Sunnyvale, CA) and cross-correlation PIV software (LaVision GmbH, DaVis 7, Goettingen, Germany). In these measurements, the droplets sprayed into the flame and the particulate matter obtained from these droplets were used as the seed. The image spanned a region of $80\,\text{mm} \times 135\,\text{mm}$ downstream of the flame nozzle. Velocity fields were extracted from 40 PIV images and they were averaged to obtain the time-averaged velocity field.

The spray droplet sizes and velocities were measured by a phase-Doppler particle anemometer (Aerometrics Inc, Composed of Models: FBD240-R, XMT204-2.1, RCV200-V, RSA3200-L, RSA3200-P, Sunnyvale, CA) [17]. This instrument measures both droplet sizes and velocities based on the principles of the light scattering interferometry. The intersection of two laser beams of identical wavelength creates a fringe pattern within the probe volume, characteristics of which are only dependent on the laser wavelength and optical configuration. As a droplet passes through the probe volume, laser beams are scattered from the droplet surface and a fringe pattern is projected onto the collection optics where a lens focuses the image onto several detectors. The receiver of the system is positioned at an off-axis location, which was set at 150° from the transmitter axis in this case. Doppler burst signals are received from individual detectors and the frequency of the bursts can be transformed into velocity since the fringe spacing is only a function of the laser wavelength and optical configuration. Also, the phase shift between the Doppler burst signals detected by different detectors is related to

the size of the droplet, and size can be measured by assuming the droplets are spherical (which holds true for water droplets smaller than 400 μm).

Sampling of the droplets and/or particulates from the flame was accomplished using a pneumatic double-acting piston arrangement driven by a double-acting solenoid valve. The solenoid valve was controlled by a time delay unit. Samples were collected on small copper substrates ($32\,\text{mm} \times 25.4\,\text{mm} \times 1.6\,\text{mm}$ thick) with a typical sampling time of 100 ms in the flame. Samples were collected at 2, 4 and 6 cm downstream locations to study the evolution of ceramic formation in the flame. At each location, two different sample collection schemes were employed. In impact sampling mode, the substrate was inserted perpendicular to the flame axis. This enabled collection of larger droplets and/or particulates due to the larger momenta of these particles impacting onto the substrate. In the thermophoretic sampling technique, the substrate was inserted parallel to the flame axis to facilitate collection of smaller particulates. Thermophoresis due to temperature gradients and turbulent velocity fluctuations within the flame allowed more gentle attraction of these smaller particulates onto the substrate. Collected samples were subsequently analyzed using an environmental scanning electron microscope (ESEM) for the morphology and Raman scattering for the phase analysis.

3. Results and discussion

In the generation of the droplet spray, a miniature air-blast atomizer was used. Characterization of the spray was performed by the phase-Doppler particle analyzer system that acquired 20,000 simultaneous droplet size and velocity measurements. The typical distributions of droplet size and velocity for this type of atomizer are shown in Fig. 3. The droplet size ranges in a relatively narrow distribution between 1 and 20 μm as depicted in Fig. 3(a) with a number averaged diameter of about 10 μm.The droplet velocities, shown in
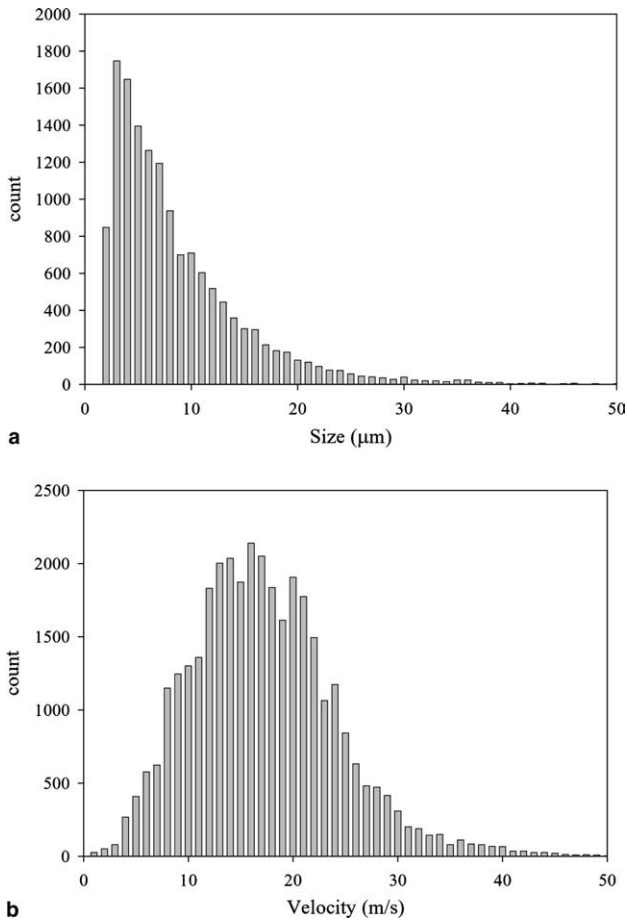
Fig. 3. Phase-Doppler particle analyzer results of (a) droplet size, and (b) droplet velocity distributions generated by the miniature air-blast atomizer.

Fig. 3(b), ranged mostly between 5 and 30 m/s. The number averaged droplet velocity was measured to be 16 m/s.

Next, the thermal and flow field characteristics of the oxy-acetylene flame were determined followed by the material characterization of the deposits. The thermal environment of the flame was characterized by gas temperature measurements using the aforementioned spectroscopic technique. The flame OH chemiluminescence emission distributions were captured by an imaging spectrometer and they were deconvoluted into localized radial distributions using a two-point Abel's inversion technique [16]. The temperature distribution is shown for the $\phi = 1.1$ flame in Fig. 4(a) without the nitrogen flow through the atomizer. Highest temperatures in the flame were found at around 3 mm downstream of the flame within three pockets. These pockets are a manifestation of six small premixed flames emanating from the nozzle. These individual flames influence the symmetry of the temperature field at these upstream locations. For example, the maximum temperature zones appear as pockets within the temperature field. Highest temperatures that were recorded in the flame were about 4300 K. This value compares with 5500 K obtained from chemical equilibrium computation which does not account for the radiative heat loss from the flame [18]. The measured temperatures decrease to about 1000 K at around 65 mm downstream of the nozzle. These temperatures were obtained without the spray and atomizing nitrogen gas introduced into the nozzle. The typical accuracy of the spectroscopic temperature measurements was estimated to be between 1% and 3% for high and low temperatures, respectively. In the actual process with the droplet spray, the flame temperatures are modified due to the nitrogen flow through the atomizer as well as the droplet vaporization during the heat up of the precursor. Introduction of the liquid atomizing nitrogen gas resulted in reduction of the temperatures by about 1000 K as seen in Fig. 4(b). The ef-
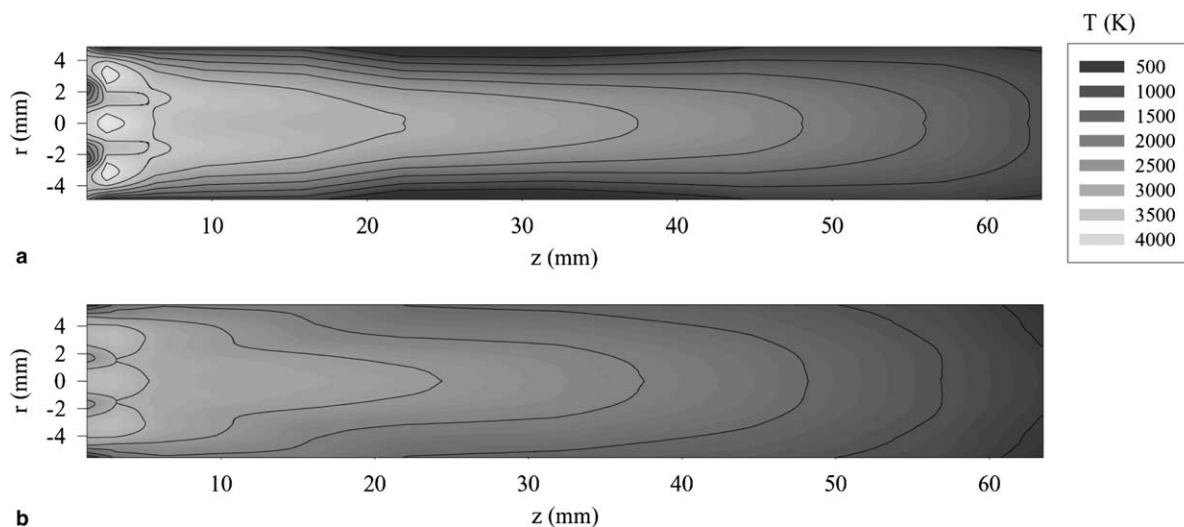

Fig. 4. Measured temperature fields (a) for the oxygen–acetylene mixture with an equivalence ratio $\phi = 1.1$; and (b) for the same flame composition with nitrogen flow through the spray nozzle at the same flow rate as that employed in the spray experiments.

fects of the atomizing nitrogen gas flow were more pronounced at the upstream locations. The highest temperatures were reduced to about 3300 K. Also, the temperature distribution was found to be altered in the radial direction due to the nitrogen flow. However, the downstream temperature profiles were not affected considerably. The temperatures were of the order of 1000 K at 65 mm downstream of the flame with temperature decay being mostly controlled by jet entrainment. The effect of liquid water vaporization on the thermal environment was estimated based on a simple energy balance. Based on the liquid and gas flow rates employed in the experiments, a temperature drop of about 300 K was calculated for total evaporation of liquid stream in the flame. This is smaller than the effect of liquid atomizing nitrogen as discussed earlier.

The measured flame temperatures along the flame centerline are similar to those along the trajectory of transversely injected droplets into the plasma [10]. However in the plasma, the droplets initially traverse the colder outer regions, and the temperatures increase as the droplets penetrate into the plasma. For the plasma, the heating rate along droplet trajectory is in the range of 10^5–10^7 K/s. On the other hand, in the flame experiments, the initial temperatures are high, and the temperatures eventually decay due to jet entrainment and radiative losses. The decay in the temperature along the axis of the flame nozzle is more or less steady at 10^6 K/s. Based on the trajectories of the droplets in the plasma and in the flame, the residence time of the droplets at high temperatures in the flame is longer than those injected into the plasma jet transversely.

Velocity measurements were carried out by the particle image velocimetry system described earlier. The precursor solution droplets and the in-flame formed particulates were illuminated by the double-pulsed Nd:YAG laser during which two images of the flame were taken. The cross-correlation of the two images yield a displacement field and the associated velocities. The average velocity field obtained by averaging 40 individual velocity maps is shown in Fig. 5. It was seen that the velocities in the gas stream reach as high as 70 m/s. Highest velocities were observed at around 15–30 mm downstream of the flame nozzle after which the velocities decayed. A close-up of the near nozzle region is shown in Fig. 5(b), clearly exhibiting the initial acceleration and subsequent decay in the core velocities. This is expected since the injected droplets are large enough to lag in their approach to the local gas velocity initially. Upon vaporization and reduction in size, the seed particles follow the gas flow more closely. The downstream decay of velocities is due to the ambient air entrainment. The standard deviation of the instantaneous velocities from the mean (shown in Fig. 5) was also calculated as shown in Fig. 6. It is seen that the maximum variations were below 5 m/s at the flame core where typical
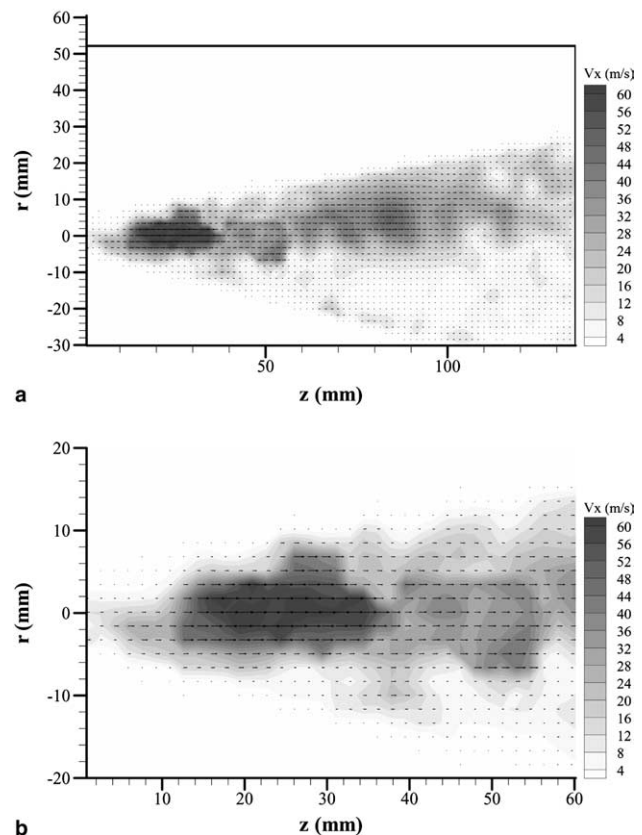

Fig. 5. Measured velocity field for the oxygen–acetylene mixture with an equivalence ratio $\phi = 1.1$ and with the droplet generation: (a) overall field; (b) near nozzle region.

velocities were about 70 m/s. This shows less than about 7% variation in the instantaneous velocities. Standard deviation increases at farther downstream locations (ca. 130 mm downstream) and jet boundaries since mixing results in significant variations in the local velocities.

In order to estimate axial velocity near the spray nozzle, the velocities were calculated invoking the mass conservation and using the temperature distribution with the assumption of negligible radiative losses and assumption that the temperature decay is being strictly associated with jet mixing. Conservation of energy and momentum under the assumption of constant specific heats results in

$$\frac{V(z)}{V(0)} = \frac{T_{CL}(z) - T_\infty}{T_{CL}(0) - T_\infty}. \tag{2}$$

In this equation, $V(z)$ is the centerline velocity along the flame axis, $T_{CL}(z)$ is the measured centerline temperature and T_∞ is the ambient temperature at which the entrained air is introduced into the flame. Based on this relation, the centerline temperature and centerline velocity are shown in Fig. 7. From the acetylene, oxygen and atomizing gas mass flow rates, the initial velocity, $V(0)$, was estimated to be around 90 m/s. The estimated velocities show some discrepancy at upstream locations.
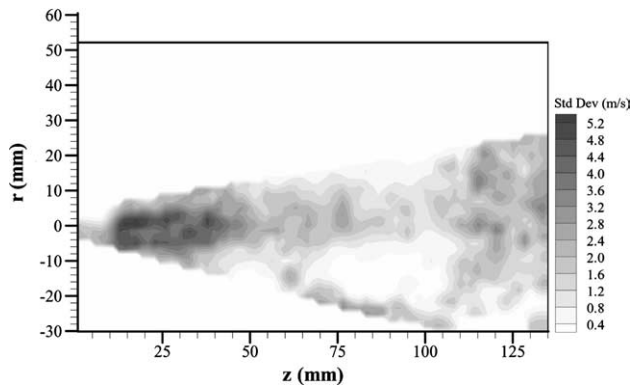
Fig. 6. Standard deviation in the measured velocity field for the oxygen–acetylene mixture.

However, good agreement is observed between the measured and predicted velocities after about 30 mm downstream. In Fig. 7, the trend of measured velocity shows a region of almost constant droplet velocities up to 10 mm followed by an acceleration zone extending to about 20 mm. This behavior is a result of the inner droplet jet stream mixing with the higher velocity outer flow stream of the flame. The coaxial jet mixing begins to penetrate into the core droplet stream at around 10 mm distance and accelerates the droplets/particles to the outer stream velocity by 20–30 mm distance downstream of flame nozzle.

The residence times for the droplets were calculated from the integration of the velocity measurements as $\tau_r(z) = \int_0^z \frac{dz}{V(z)}$. In Fig. 7, the top axis shows the residence time for droplets in the high temperature environment. Typical residence times were about 2.5 ms on axis of the flame. Similar calculations were carried out for 5° and 10° angle rays originating from the nozzle exit to account for the cone spray angle. The residence times versus temperature are shown in Fig. 8 along the centerline, 5° and 10° rays. Along the flame

axis, the gas velocities are higher and therefore the residence times for these droplets are slightly shorter than those that are injected at 5° angle from the centerline. These droplets also travel slower than the centerline droplets, therefore they are exposed to high temperatures for longer times. On the other hand, 10° injection angle results in lower temperatures since the wider angle injection throws these droplets into the cooler outer regions of the flame.

Samples collected from the flame contain useful information on the particle morphologies as well as their composition. Samples were collected at 2, 4 and 6 cm from the flame nozzle using impact and thermophoretic sampling techniques described earlier. SEM micrographs of impact samples are shown in Fig. 9. Fig. 9(a) and (b), collected at 2 and 4 cm locations, show similar structures, both being larger deposits spreading over the substrate. These formations are reminiscent of droplets containing liquid precursor, particularly the hemispherical structure in Fig. 9(a). Here, one can see that the average splat size is about 30–35 µm, which was generated from droplet sizes of 1–20 µm upon impact. However, other samples collected at 4 cm location contain fine spherical structures as shown in Fig. 9(c). The structures change into fine particulates as one proceeds downstream to 6 cm location in Fig. 9(d). The progression of the obtained morphologies showed that smaller formations are observed with increasing downstream locations. In Fig. 10, thermophoretic samples collected at 2 and 4 cm location are shown. These samples were similar to each other, regardless of the sampling location, showing some semi-processed material structure which may result from rapid precipitation processes indicated by the small loosely bonded structures. One should note that the substrate surface features seen in both impact samples (Fig. 9) and thermophoretic samples (Fig. 10) are not due to the flame exposure,
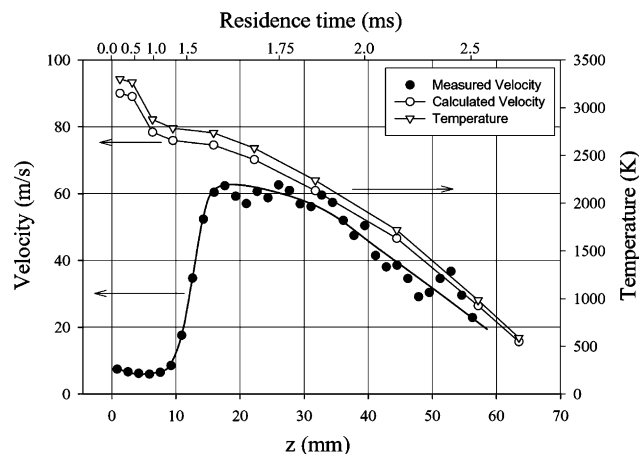

Fig. 7. Theoretical velocity distribution at the axis of the flame nozzle calculated from temperature distribution compared to the measured centerline velocity.
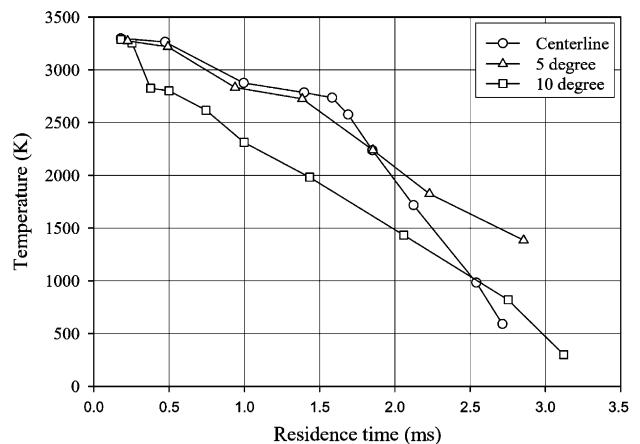

Fig. 8. Residence times and corresponding temperatures along the axis of the flame as well as at 5° and 10° directions.
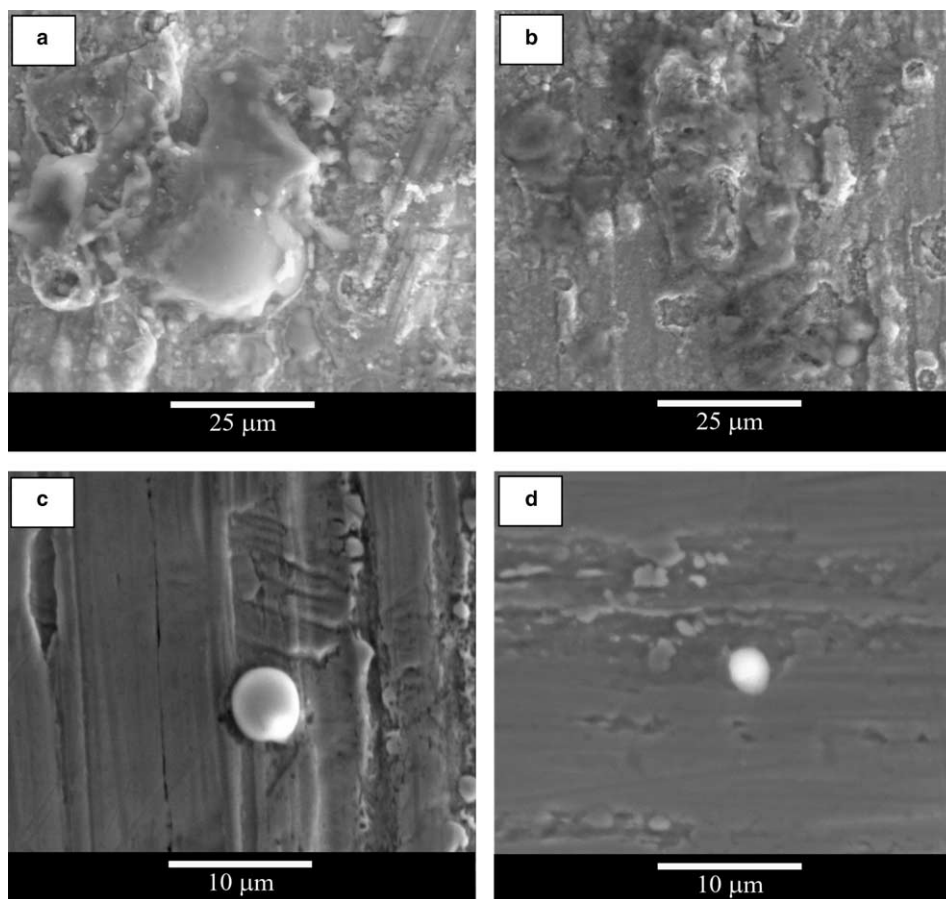
Fig. 9. ESEM images of impact samples (a) at 2 cm, (b,c) at 4 cm, and (d) at 6 cm downstream of the flame nozzle.

but are the surface roughness features of the substrates used.

In order to verify the formation of yttria-stabilized zirconia in the flame, multiple insertion samples were generated on copper coupons. The substrates were inserted into the flame similar to the impact samples and thicker deposits were collected to perform Raman analysis on these samples. The Raman shift spectra shown in Fig. 11, indicate the presence of the yttria-stabilized zirconia in the deposit. Peaks of the meta-stable tetragonal t'-phase were observed in the 100–1000 cm^{-1} range. These peaks were found to become stronger with increasing downstream distance due to longer residence times for precursor decomposition and YSZ formation. Spectral peaks for CH_3 and COO groups are also present in the spectra. However, the peaks associated with these organic groups in the precursor decreased as the residence times increased and at 6 cm location only a small peak of CH_3 remained at around 3100 cm^{-1}.
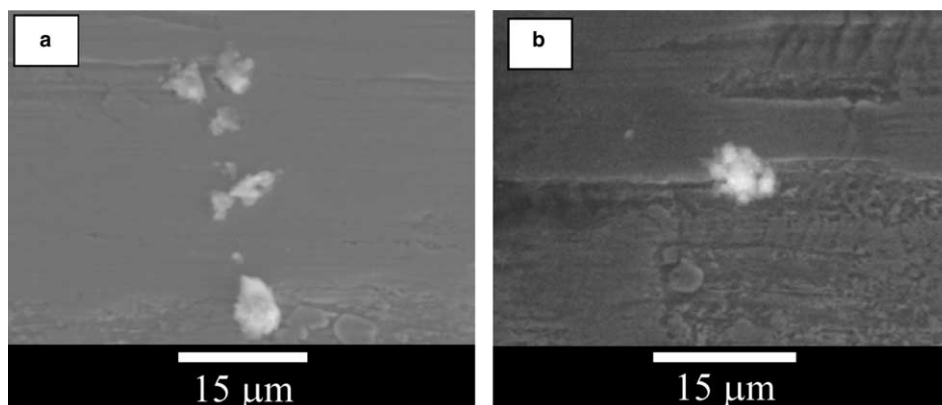

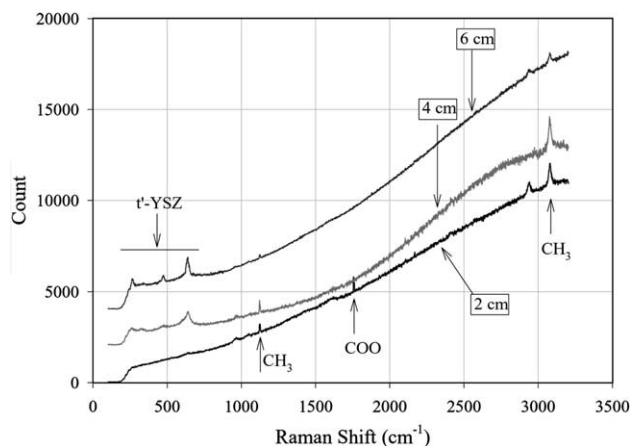Fig. 10. ESEM images of thermophoretic samples (a) at 2 cm and (b) at 4 cm downstream of the flame nozzle.

Fig. 11. Raman shifts obtained from multiple-insertion of copper substrates into the flame.

4. Concluding remarks

A study of the liquid precursor droplet transformation into ceramic material in an oxygen–acetylene flame environment was performed. The flame temperature field was characterized by a spectroscopic temperature measurement technique using the rotational band of the hydroxyl radical present in the flame. The flame temperature distributions were measured to fully characterize the flame thermal environment. Droplet velocity distribution in the flame field was investigated using the particle image velocimetry and phase-Doppler anemometry techniques. The measurements were found to be consistent with calculations invoking simplified version of the conservation of energy and momentum. The morphology and phase of the droplets/particulates within the flame were studied from samples extracted by using impact and thermophoretic sampling techniques. These samples were analyzed using the scanning electron microscopy and Raman spectroscopy. As the residence time increases in the flame (in terms of location in the flame), smaller ceramic particulates were formed. Typical residence time for ceramic formation in the flame was found to be between 2 and 3 ms. Thick deposit samples were analyzed and it was determined that the deposits contain increasing amounts of t'-phase of yttria-stabilized zirconia with increasing downstream distance.

Acknowledgments

References

[1] Miller RA. Surf Coat Technol 1987;30:1–11.
[2] Evans AG, Mumm DR, Hutchison JW, Meier GH, Pettit FS. Prog Mater Sci 2001;45:505–53.
[3] Padture NP, Gell M, Jordan EH. Science 2002;296:280–4.
[4] Padture NP, Schlichting KW, Bhatia T, Ozturk A, Cetegen BM, Jordan EH, et al. Acta Mater 2001;49:2251–7.
[5] Xie L, Ma X, Jordan EH, Padture NP, Xiao TD, Gell M. Mater Sci Eng 2003;A362:204–12.
[6] Xie L, Ma X, Ozturk A, Jordan EH, Padture NP, Cetegen BM, et al. Surf Coat Technol 2004;183:51–61.
[7] Xie L, Ma X, Jordan EH, Padture NP, Xiao DT, Gell M. Surf Coat Technol 2004;177–178:103–7.
[8] Bhatia T, Ozturk A, Xie L, Jordan EH, Cetegen BM, Gell M, et al. Mater Res 2002;17:2363–72.
[9] Ozturk A, Cetegen BM. Acta Mater 2005;53:2531–44.
[10] Ozturk A, Cetegen BM. Mater Sci Eng 2004;A384:331–51.
[11] Ozturk A, Cetegen BM. Modeling of axially and transversely injected precursor droplets into a plasma environment. Int J Heat Mass Transfer 2005;21–22:4367–83.
[12] Turns SR. An introduction to combustion: concepts and applications. New York, NY: McGraw-Hill; 2000.
[13] Tageldin MS, Cetegen BM. Combust Sci Technol 1997;130: 131–69.
[14] Pellerin S, Cormier JM, Richard F, Musiol K, Chapelle J. J Phys D: Appl Phys 1996;29:726–39.
[15] Dieke GH, Crosswhite HM. J Quant Spectrosc Radiat Transfer 1962;2:97–199.
[16] Dasch C. J Appl Opt 1992;31:1146–52.
[17] Bachalo WD, Houser M. J Opt Eng 1984;23:583–90.
[18] Reynolds W. Stanjan: chemical equilibrium code. California: Stanford University; 1980.